ChemPubSoc Europe

DOI: 10.1002/chem.201403171

CHEMISTRY
A European Journal
Communication

Molecular Motors

Catalytic Self-Propulsion of Supramolecular Capsules Powered by Polyoxometalate Cargos

Loretta L. del Mercato,*[a] Mauro Carraro,*[b] Alessandra Zizzari,[a] Monica Bianco,[a] Ruggero Miglietta,[a] Valentina Arima,[a] Ilenia Viola,[a] Concetta Nobile,[a] Antonio Sorarù,[b] Debora Vilona,[b] Giuseppe Gigli,[a, c] Marcella Bonchio,*[b] and Rosaria Rinaldi[a, c]

Abstract: Multicompartment, spherical microcontainers were engineered through a layer-by-layer polyelectrolyte deposition around a fluorescent core while integrating a ruthenium polyoxometalate (Ru_4POM), as molecular motor, vis-à-vis its oxygenic, propeller effect, fuelled upon H_2O_2 decomposition. The resulting chemomechanical system, with average speeds of up to 25 $\mu m\,s^{-1}$, is amenable for integration into a microfluidic set-up for mixing and displacement of liquids, whereby the propulsion force and the resulting velocity regime can be modulated upon H_2O_2-controlled addition.

The transduction of chemical energy into mechanical motion has a major appeal in terms of powering nano-to-microscale systems, or part of them, with molecular control.[1] The core concept is the role of the so-called functional actuators, that is, chemical systems that respond to reagents/stimuli at the molecular level (input) and produce a mechanical effect (output), propagating from the molecular to the macroscale, while exhibiting high specificity, long-range operation, and reversibility. Chemomechanical strategies are known to play a key role in natural machineries and often involve enzymatic processes as functional actuators.[2] Enzymes have also been applied under artificial environments as catalytic chemomechanical actuators. In particular, the oxygenic activity of natural catalases can induce self-propulsion of synthetic objects using H_2O_2 as chemical fuel. Catalase enzymes effect H_2O_2 disproportionation ($2\,H_2O_{2(l)} \rightarrow 2\,H_2O_{(l)} + O_{2(g)}$), liberating nascent oxygen gas with a resulting propulsion effect. Autonomous movement of nano/microobjects can thus be triggered by tailored bioconjugates, integrating such oxygenic enzymes.[3] With a similar approach, catalase mimetics (based on dimanganese(II) complexes,[4] metallic Pt,[5] or Ni[6] particles) have been reported as catalytic propellers. H_2O_2-fuelled nano- and micromotors have potential applications for cargo delivery, imaging and trafficking in synthetic circuits as well as in biological media. In this perspective, a tailored choice of the catalytic propeller and of the surrounding material/morphology is pivotal to tune velocity, performance, and robustness.

We present herein the hierarchical assembly of multilayer polyelectrolyte capsules,[7] integrating a fluorescent tag, and armed with a H_2O_2 disproportionation catalytic trigger. This latter is the tetrasubstituted Ru^{IV} polyoxometalate, with the formula $Na_{10}[Ru_4(H_2O)_4(\mu\text{-}O)_4(\mu\text{-}OH)_2(\gamma\text{-}SiW_{10}O_{36})_2]$ (Ru_4POM), the catalase-like activity and propeller function of which have been recently reported in aqueous phase.[8] Our approach builds on the vast knowledge of the supramolecular chemistry of anionic POMs, evolving to complex systems by electrostatic interactions with positively charged interfaces.[9] The selective confinement of oxygenic Ru_4POM has thus been obtained within the positive shells of polymeric containers,[10] which turn out to respond to H_2O_2 by displaying long-lasting and reversible catalytic motility with speeds of up to 25 $\mu m\,s^{-1}$ and propulsion forces approaching 1 pN with a catalyst loading as low as 0.5 fmol per capsule (Figure 1). Compared to state-of-the-art chemomechanical micromotors,[3–6] our results combine the key advantages of employing: 1) a robust, multiturnover and molecular inorganic synzyme, 2) a straightforward fabrication strategy which exploits multiple electrostatic interactions, 3) a multicompartment container for targeted delivery/transport/imaging. By virtue of its molecular and supramolecular character, the resulting chemomechanical system offers a valuable adaptive potential in terms of catalyst loading and hierarchical architecture to fit a wide range of conditions/environments for selected applications. We address here its transposition to a microfluidic set-up, where the bulk effect of fluid displacement induced by the catalytic micromotors can be monitored and modulated upon H_2O_2 controlled addition.

The polyelectrolyte capsules were hierarchically assembled by layer-by-layer (LbL)[7] adsorption of poly(styrenesulfonate) (PSS) and polyallylammonium hydrochloride (PAH). These polyelectrolytes, with opposite charges, were sequentially deposited onto a sacrificial calcium carbonate ($CaCO_3$) template integrating a dextran–rhodamine (dextran-RITC) dopant, yielding

[a] Dr. L. L. del Mercato, A. Zizzari, Dr. M. Bianco, R. Miglietta, Dr. V. Arima, Dr. I. Viola, Dr. C. Nobile, Prof. G. Gigli, Prof. R. Rinaldi
NNL, Nanoscience Institute-CNR
Via Arnesano, 16, 73100 Lecce (Italy)
E-mail: loretta.delmercato@nano.cnr.it

[b] Dr. M. Carraro, A. Sorarù, D. Vilona, Prof. M. Bonchio
ITM-CNR and Department of Chemical Sciences
University of Padova, Via Marzolo, 1, 35131 Padova (Italy)
E-mail: mauro.carraro@unipd.it
marcella.bonchio@unipd.it

[c] Prof. G. Gigli, Prof. R. Rinaldi
Department of Mathematics and Physics "Ennio De Giorgi"
University of Salento, Via Arnesano, 73100 Lecce (Italy)

Supporting information for this article is available on the WWW under http://dx.doi.org/10.1002/chem.201403171.

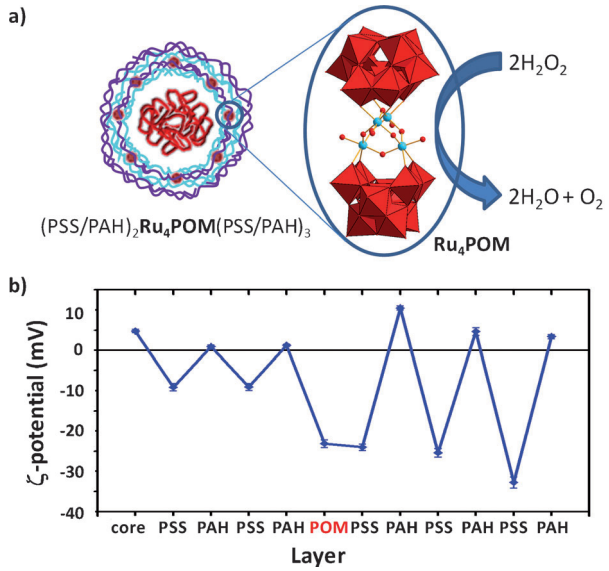

Figure 1. a) Illustration of the composition of a polyelectrolyte multilayer capsule carrying dextran-RITC into the cavity (red bundle) and Ru_4POM complexes (red spots) into the multilayer shell (left); Ru_4POM structure and its catalase-like reactivity (right); b) ζ-potentials variations during $CaCO_3$ particles coating with PSS, PAH and Ru_4POM layers.

a multilayer core-shell particle (Scheme S1 in the Supporting Information). With this protocol, loading of Ru_4POM, as decaanion, was readily achieved after the fourth positive PAH layer. Direct evidence of the POM uptake comes from the color change of the loaded pellets, which turned brown upon a single exposure to the Ru_4POM solution (Figure S1 in the Supporting Information).

The efficient uptake of the catalyst was confirmed by UV/Vis analysis of the Ru_4POM solution (H_2O, pH 5.0, 2 mg mL^{-1}, 0.35 mM), showing a more than 80% decrease ($\lambda = 270$ nm; $\varepsilon = 74846$ mol L^{-1} cm^{-1}) when incubated with the polymeric capsules (see the Supporting Information for details).

The oxygen-evolving POM turned out to be confined within the multilayer shells, according to a $(PSS/PAH)_2Ru_4POM(PSS/PAH)_3$ arrangement (Figure 1 a). The alternating charge deposition is conveniently monitored, along the fabrication process, by ζ-potential analysis (Figure 1 b), performed after each polyelectrolyte coating. Along the build-up of the multilayer shell, ζ-potential values show an oscillating response on sequential addition of PSS (up to −35 mV), PAH (up to +10 mV) and Ru_4POM (−23.1 mV). In its final arrangement, the multilayer capsule features a slightly positive surface charge (up to +4 mV). Reproducible ζ-potential profiles were collected for different fabrication batches (Figure S3 in the Supporting Information). As a final step, the carbonate template was dissolved with 0.2 M EDTA at neutral pH, thus leaving a dextran–RITC luminescent filler in the central core of the capsule, while the Ru_4POM catalytic domains are confined in the surrounding shell (see the Supporting Information).

The morphology of the resulting capsules was analyzed by fluorescence and electronic microscopies, and showed a spherical shape with an average diameter of 3–4 μm, dye-filled cavities, and multilayer shells observed as folds and cristae, formed upon solvent removal as determined by transmission electron microscopy (TEM; Figure 2 and Figures S7–S10 in the Supporting Information).

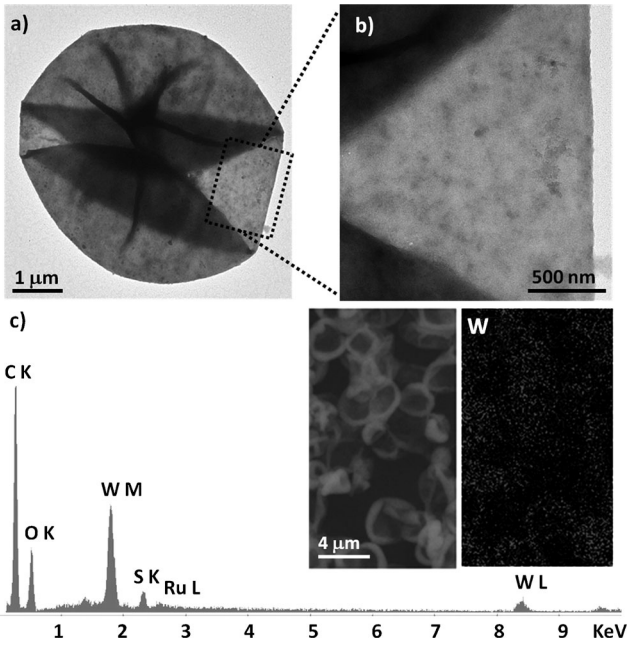

Figure 2. a) TEM images of a single $(PSS/PAH)_2Ru_4POM(PSS/PAH)_3$ capsule after core removal, and b) the magnified image of the area marked in (a), showing the integrity of the multilayer shell; c) EDAX microanalysis of the capsules (inset: ESEM images and tungsten mapping obtained by EDAX).

The confinement of the Ru_4POM cargo is assessed by three lines of evidence: 1) FT-IR spectra showing the composite features of the polymeric material and including the POM stretching bands at $\nu_{as}(W–O–W) = 804$ cm^{-1}, $\nu_s(W–O–W) = 877$ cm^{-1} and $\nu_{as}(Si–O) = 942$ cm^{-1} (Figures S4 and S5 in the Supporting Information); 2) inductively coupled plasma mass spectrometry (ICP-MS) analysis after capsule mineralization, confirming the expected W/Ru molar ratio (found: 4.5 ± 0.7, calcd: 4.0) and an overall Ru_4POM content of about 46% (w/w) on the dried material (corresponding to about 0.5 fmol per capsule; see the Supporting Information); 3) environmental scanning electronic microscopy (ESEM), coupled with energy dispersive X-ray (EDAX) analyses, mapping the heavy element distribution within the capsule outer shells. This is highlighted by the bright contour profiles of EDAX/ESEM superimposable images (Figure 2 c and Figure S9 in the Supporting Information) indicating that the tungsten sites of the POM catalyst are localized at the peripheral rim of the spherical microstructure, with an even distribution and in agreement with the fabrication planning (Scheme S1 in the Supporting Information).

Diffusion of H_2O_2 to the catalytic sites of the capsule occurs through its polyelectrolyte shells that are known to be permeable to small molecules.[11] H_2O_2 is then expected to be a chemical trigger for nascent O_2 generation, according to a second-order kinetic law, in agreement with the following equation:[8b]

$$H_2O_2 + Ru_4POM \rightarrow H_2O + 1/2\,O_2 \qquad R = k\,[H_2O_2][Ru_4POM]$$

where R is the reaction rate, and k is the second-order-reaction constant. Under homogeneous conditions (h), that is, with free catalyst in solution ($[Ru_4POM] = 3.6\ \mu M$, $[H_2O_2] = 0.1\ M$, sodium phosphate buffer 50 mM, pH 7.0), the initial rate of oxygen evolution, determined upon continuous monitoring of the pressure variation (< 15% conversion), is $R_0^h = 0.155\ mmol\,s^{-1}$, corresponding to $k^h = 36.8\ M^{-1}\,s^{-1}$.

The catalytic response of the encapsulated Ru_4POM (cap), when exposed to H_2O_2, turns out to be much slower, yielding $R_0^{cap} = 0.01\ mmol\,s^{-1}$ and $k^{cap} = 39\ \mu M^{-1}\,s^{-1}$ (Table S1 and Figure S12 in the Supporting Information). Diffusion phenomena may be envisaged for the encapsulated state as well as a strong interaction/wrapping of the Ru_4POM by the PAH polyelectrolyte that can affect equilibria and solvation of the reactive states. Indeed, progressive addition of PAH (0.02–0.2 $mg\,mL^{-1}$) to a homogeneous Ru_4POM solution (3.6 μM) is responsible for a corresponding abatement of the O_2 evolution rate (Table S1 and Figure S12 in the Supporting Information).

FT-IR analysis of the spent capsules, recovered after centrifugation and washing/drying cycles, shows no significant modification of the catalyst spectral features (Figure S6 in the Supporting Information). Indeed, the oxygen evolution activity can be maintained over a long time operation run, reaching 54% H_2O_2 conversion after 9 h (turnover number, TON, up to 1.5×10^4; Figure S13 in the Supporting Information).

The initial oxygen evolution burst and its steady long-time running are key phenomena that induce the autonomous motility of the microcapsules by the propelling force of the nascent gas. This catalytic chemomechanical response and its potential use as motor effector has been addressed at the microscale by considering: 1) the capsule motility as single microobjects, 2) the resultant turbulence-induced pressure, seeded by the oxygenic particles and applied for the displacement of fluids within a microchannel set-up.

Under catalytic regime, O_2 evolution within the $(PSS/PAH)_2Ru_4POM(PSS/PAH)_3$ capsule suspension can be easily observed by optical microscopy (Figure 3). Upon addition of H_2O_2 (1.23 M), the release of oxygen bubbles from the capsule surface occurs as a continuous phenomenon (videos V1 and V2 in the Supporting Information and Figure 3a and b). Time-lapse images show the formation of a long tail of oxygen bubbles (dark circles in Figure 3a and b), with average diameter < 10 μm, that coalesce into macrobubbles with diameter > 500 μm (video V2 and Figure S16 in the Supporting Information). Under catalytic regime, an efficient propulsion turbulence is thus propagating within the aqueous environment. In the images shown in Figure 3a and b, the capsules lie on the bottom of the first bubble and are not visible, being smaller and located on a different focal plane; nevertheless, the motion of numerous small particles, swimming within the suspension, can be clearly appreciated in the background (videos V1 and V2 in the Supporting Information).

Imaging of the micromotor behavior as a result of the nascent gas propeller-momentum is acquired by switching the optical microscope to the fluorescent channel, thus tracking the position and movement of the luminescent tag integrated within the capsule core (see the Supporting Information for details).

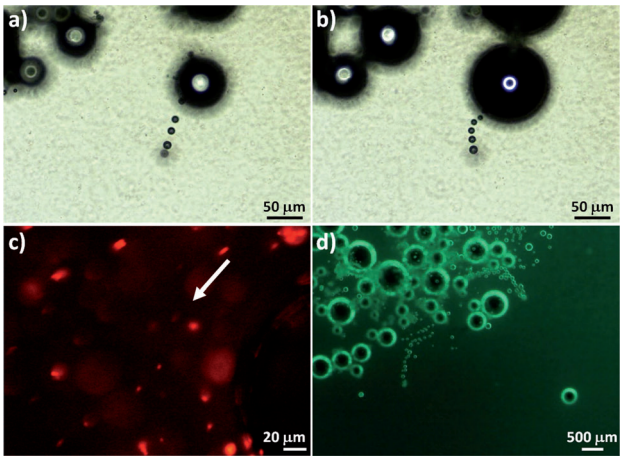

Figure 3. Optical microscopy images, showing oxygen evolution and motion of the Ru_4POM-loaded capsules upon addition of H_2O_2 (1.23 M): a), b) continuous release and coalescence of oxygen bubbles (time frame 0–54 s, video V1 in the Supporting Information), c) fluorescence tracking of capsule motion observed as red spheres (time frame 0–8 s, video V3 in the Supporting Information), d) fluorescein isothiocyanate (FITC) staining of the water suspension mixed and displaced by the turbulence-seeded phenomena due to oxygen release (video V5 in the Supporting Information).

A typical time-lapse image is shown in Figure 3c (see video V3 in the Supporting Information): $(PSS/PAH)_2Ru_4POM(PSS/PAH)_3$ capsules are imaged as red spheres and happen to be located on different focal planes. Bubble generation imparts a definite propulsion to the particle system, moving along random trajectories. The random motion is a result of the spherical distribution of the catalyst domain and of the soft material scaffold imparting some asymmetry in the oxygen jet-flow.

When observed in 1.23 M H_2O_2, the capsule displacement occurs along linear or circular trajectories (see videos V3 and V4 in the Supporting Information) with speeds of up to 25 $\mu m\,s^{-1}$. This corresponds to a calculated driving force of at least 0.94 pN per particle, according to the equation $F = 6\pi\mu a v_c$, considering a spherical colloidal model with radius $a \geq 2$ μm, while v_c is the average speed of the capsule micromotor and μ is the viscosity of water.[5b]

A remarkable local force is thus exerted by O_2 streaming from the capsule shells as a long-lasting continuous flow, which has been exploited for liquid-mixing and self-propulsion in a microfluidic device. The active mixing of the fluid, and the turbulence-seeded phenomena, are highlighted by fluorescein isothiocyanate (FITC) staining of the water suspension containing Ru_4POM-loaded capsules after addition of H_2O_2 (Figure 3d and video V5 in the Supporting Information). The behavior of the catalytic micromotors, and their H_2O_2 fuelled propulsion effect,[5b,11b] were studied under capillary-driven fluidodynamic conditions[12] (Figure 4, see the Supporting Information for details). According to the experimental set-up (Figure 4a), the flow dynamics under catalytic oxygen evolution are measured

in real time within a microchannel, at different H_2O_2 concentrations, in the range 0–1.23 M. The experimental space-time coordinates (z,t) were detected instantly for each sample and are reported as the displacement lengths of the fluid inside the channel (Figure 4b and c).

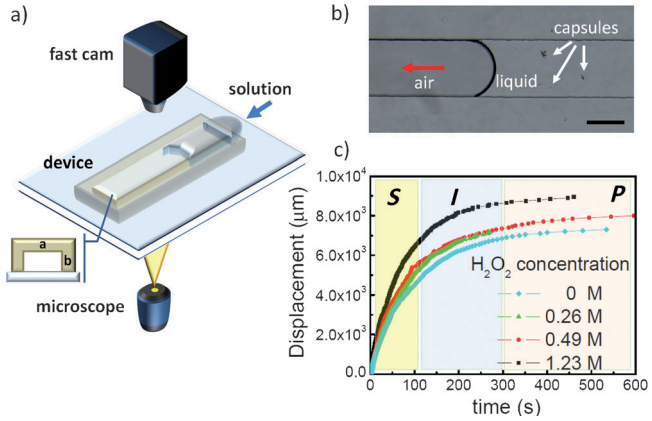

Figure 4. a) Sketch of the fluidic device and of the measuring set-up (channel section with $a = 150$ μm and $b = 20$ μm); b) optical micrograph of the channel during the fluidic process (scale bar: 100 μm); c) fluid displacement lengths versus time. Each curve corresponds to the injection of solutions with $[H_2O_2] = 0$, 0.26, 0.49 and 1.23 M. The starting (*S*), intermediate (*I*) and plateau (*P*) regime of the solution dynamics are highlighted in the plot.

Since the fluid behavior is affected by some critical parameters, such as solution temperature,[13] the mixing/deposition time, and the presence of capsule agglomerates, these parameters were carefully controlled for the different experiments to allow the acquisition of reproducible curves (Figure S17 in the Supporting Information) and trends (Figure S18 in the Supporting Information). The analytical expression of the fluid displacement in a microchannel follows a power-law dynamics, known as Washburn's law, which takes into account the confinement boundaries of the microchannel shells.[14]

According to this law, three different regimes can be distinguished defined as starting (*S*), intermediate (*I*) and plateau (*P*), depending on the observation timeframe (Figure S19 in the Supporting Information and Figure 4c).[12,13] The floating micromotors affect the fluidic process and its capillary dynamics, by a complex interplay of factors including: the size and rate of bubble formation, the size and number of the oxygen evolving seeds on the particle surface, the finite size of the particles suspended in the liquid and its viscosity.[15] We expect that the bimolecular catalytic event is herein the major driving force to sustain the bubble-induced velocity fluctuation and turbulent flow. Indeed, fitting of the experimental curves of Figure 4b, shows that, while in the absence of H_2O_2 the flow dynamics of the starting regime (*S* zone, time interval of about 100 s) corresponds to a pure capillarity behavior, increasing the H_2O_2 concentration imparts a remarkable flow acceleration, which turns out to be dependent on H_2O_2 concentration. The perturbation of the capillary dynamics can be calculated for each solution (see the Supporting Information) considering the maximum fluid velocity. The velocity (v) of the solution front increases with the H_2O_2 fuel amount, added to the capsule solution, from the ground value of $v = 85$ μm s^{-1} at 0 M H_2O_2, going to $v = 89$, 100 and 160 μm s^{-1}, respectively, at 0.26, 0.49, and 1.23 M H_2O_2. The observed dependence of the fluid velocity on the added H_2O_2 parallels the oxygen evolution rate (R_0), experimentally determined as a function of the H_2O_2 concentration (Figure 5 and Figures S14 and S15 in the Supporting Information). This behavior confirms that the catalytic event by the Ru_4POM effector is the dominating factor to control the chemomechanical response of the particle system under microfluidic regime, thus providing a convenient tool for the optimization of tailored devices.

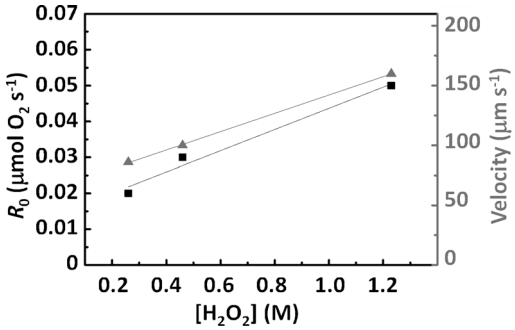

Figure 5. Dependence of the fluid velocity displacement (triangles) by oxygenic microcapsules on added $[H_2O_2]$ under microfluidic regime, and parallel behavior of the oxygen evolution rate (squares) under catalytic turnover.

In conclusion, the confinement of the synthetic catalase, Ru_4POM, offers an unprecedented tool for the supramolecular engineering of catalytic microcarriers exhibiting autonomous movement and propulsion effect with H_2O_2 as fuel. Their modular fabrication and molecular components allow a precise control of both the loading of the catalytic effector and of its positioning by a tailored design of the structure and numbers of the hierarchical layers/compartments.

As a corollary, the mechanical pressure of nascent oxygen and the associated force momentum can affect the capsule stability and produce an irreversible collapse of their multilayer shells. This possibility has been addressed by TEM imaging of the spent particles recovered after oxygen evolution, where some capsules appear broken (Figure S8 in the Supporting Information). Since the capsule shells can be tuned in terms of composition and layered structure,[7] the remote control of their opening and subsequent cargo-release may be relevant for smart-drug trafficking in biological environment which is the object of current investigation in our laboratories.

Experimental Section

Layer-by-layer assembly of Ru_4POM-functionalized polyelectrolyte capsules

Dried $CaCO_3$ particles (20 mg) were suspended in 0.5 M NaCl (1 mL) solution containing the polyanion PSS (2 mg mL^{-1}, pH 6.5). The excess polyanion was removed by three centrifugation/washing

steps with 1 mL of MilliQ H_2O (1358 g for 5 s). Subsequently, 0.5 M NaCl solution (1 mL) containing the polycation PAH (2 mg mL^{-1}, pH 6.5) was added to the particles and the dispersion was mixed and treated as described above. After the deposition of the fourth layer, the particles were incubated in Ru_4POM (1 mL) solution (H_2O, pH 5.0, 2 mg mL^{-1}, 0.35 mM). Three bilayers of (PSS/PAH) were then adsorbed to complete the multilayer shells composition (PSS/PAH)$_2$Ru$_4$POM(PSS/PAH)$_3$. The sacrificial $CaCO_3$ compartments were finally removed by complexation with EDTA buffer.

Capsule characterization and evaluation of oxygenic behavior

ζ-Potential analysis was used to monitor the alternate charge layered structure, the microspherical morphology was assessed by microscopy evidence, while catalyst confinement was confirmed by combined FT-IR, UV/Vis spectra, ICP-MS analysis and oxygen evolution kinetics. Fluorescence imaging was exploited to track the capsule motion fuelled by H_2O_2 with average speeds of up to 25 μm s^{-1} and propulsion forces approaching 1 pN with a catalyst loading as low as >0.5 fmol per capsule. Catalytic activity of (PSS/PAH)$_2$Ru$_4$POM(PSS/PAH)$_3$ capsules was monitored using a home-made pressure sensor adapted for a 25 mL vial. The initial reaction rate R_0 was measured by calculating the slope of the kinetic trace at $<15\%$ conversion.

Microfluidics set-up and analysis

The fabrication of the PDMS/glass hybrid device was performed in several steps, using the soft-lithography technique. To perform the microfluidic experiments, a drop (200 μL) of freshly prepared 0.26, 0.49 and 1.23 M H_2O_2 solutions was deposited at the PDMS/glass hybrid device inlet. Three sets of measurements were performed for each experiment, run with two different batches of freshly prepared capsules. The structural parameters were derived by nonlinear regression fitting, from experimental data recorded on several trajectories of independent samples, for each solutions.

Further details about the synthesis and characterization of Ru_4POM-loaded capsules and microfluidics analyses are given in the Supporting Information.

Acknowledgements

Financial support from Fondazione Cariparo (Nanomode Progetti di Eccellenza 2010), MIUR (PRIN contract No. 2010N3T9M4, FIRB RBAP11C58Y, FIRB RBAP11-ETKA_006), Dhitech S.c.a.r.l. (project PON 01_02342 "RINOVATIS", and FP7-SACS-2013 project), are gratefully acknowledged. R.R. is grateful to IIT for partial support. A.S. gratefully acknowledges the financial support from the CARIPARO Foundation within the "Progetto Dottorati di Ricerca 2013". The ESF COST action 1203 (PoCheMoN) is acknowledged.

Keywords: microfluidics · microreactors · molecular motors · polyoxometalates · supramolecular chemistry

[1] a) A. C. V. Balzani, M. Venturi, *Molecular Devices and Machines: A Journey into the Nanoworld*, Wiley-VCH, Weinheim, **2004**; b) W. Gao, A. Pei, J. Wang, *ACS Nano* **2012**, *6*, 8432 – 8438.
[2] K. Kinbara, T. Aida, *Chem. Rev.* **2005**, *105*, 1377 – 1400.
[3] D. Pantarotto, W. R. Browne, B. L. Feringa, *Chem. Commun.* **2008**, 1533 – 1535.
[4] J. Vicario, R. Eelkema, W. Browne, A. Meetsma, R. La Crois, B. Feringa, *Chem. Commun.* **2005**, 3936 – 3938.
[5] a) D. Wilson, R. Nolte, J. van Hest, *Nat. Chem.* **2012**, *4*, 268 – 274; b) Y. Wu, Z. Wu, X. Lin, Q. He, J. Li, *ACS Nano* **2012**, *6*, 10910 – 10916; c) B. Dong, T. Zhou, H. Zhang, C. Y. Li, *ACS Nano* **2013**, *7*, 5192 – 5198; d) R. Ismagilov, A. Schwartz, N. Bowden, G. Whitesides, *Angew. Chem.* **2002**, *114*, 674 – 676; *Angew. Chem. Int. Ed.* **2002**, *41*, 652 – 654; e) T. Kline, W. Paxton, T. Mallouk, A. Sen, *Angew. Chem.* **2005**, *117*, 754 – 756; *Angew. Chem. Int. Ed.* **2005**, *44*, 744 – 746; f) W. F. Paxton, K. C. Kistler, C. C. Olmeda, A. Sen, S. K. St Angelo, Y. Cao, T. E. Mallouk, P. E. Lammert, V. H. Crespi, *J. Am. Chem. Soc.* **2004**, *126*, 13424 – 13431; g) A. A. Solovev, W. Xi, D. H. Gracias, S. M. Harazim, C. Deneke, S. Sanchez, O. G. Schmidt, *ACS Nano* **2012**, *6*, 1751 – 1756; Z. Wu, Y. Wu, W. He, X. Lin, J. Sun, Q. He, *Angew. Chem.* **2013**, *125*, 7138 – 7141; *Angew. Chem. Int. Ed.* **2013**, *52*, 7000 – 7003.
[6] S. Fournier-Bidoz, A. C. Arsenault, I. Manners, G. A. Ozin, *Chem. Commun.* **2005**, 441 – 443.
[7] a) A. G. Decher, *Science* **1997**, *277*, 1232 – 1237; b) E. Donath, G. B. Sukhorukov, F. Caruso, S. A. Davis, H. Möhwald, *Angew. Chem.* **1998**, *110*, 2323 – 2327; *Angew. Chem. Int. Ed.* **1998**, *37*, 2201 – 2205; c) L. L. del Mercato, P. Rivera-Gil, A. Z. Abbasi, M. Ochs, C. Ganas, I. Zins, C. Sönnichsen, W. J. Parak, *Nanoscale* **2010**, *2*, 458 – 467; d) A. Guerrero-Martínez, S. Fibikar, I. Pastoriza-Santos, L. M. Liz-Marzán, L. De Cola, *Angew. Chem.* **2009**, *121*, 1292 – 1296; *Angew. Chem. Int. Ed.* **2009**, *48*, 1266 – 1270; e) Q. Zhao, T. P. Fellinger, M. Antonietti, J. Yuan, *Macromol. Rapid Commun.* **2012**, *33*, 1149 – 1153.
[8] a) C. Hadad, X. Ke, M. Carraro, A. Sartorel, C. Bittencourt, G. Van Tendeloo, M. Bonchio, M. Quintana, M. Prato, *Chem. Commun.* **2014**, *50*, 885 – 887; b) A. Sartorel, M. Truccolo, S. Berardi, M. Gardan, M. Carraro, F. M. Toma, G. Scorrano, M. Prato, M. Bonchio, *Chem. Commun.* **2011**, *47*, 1716 – 1718.
[9] a) Y.-F. Song, R. Tsunashima, *Chem. Soc. Rev.* **2012**, *41*, 7384 – 7402; b) P. Yin, D. Li, T. Liu, *Chem. Soc. Rev.* **2012**, *41*, 7368 – 7383.
[10] L. Gao, E. Wang, Z. Kang, Y. Song, B. Mao, L. Xu, *J. Phys. Chem. B* **2005**, *109*, 16587 – 16592.
[11] a) A. A. Antipov, G. B. Sukhorukov, S. Leporatti, I. L. Radtchenko, E. Donath, H. Möhwald, *Colloids Surf. A* **2002**, *198*, 535 – 541; b) G. B. Sukhorukov, E. Donath, S. Moya, A. S. Susha, A. Voigt, J. Hartmann, H. Mohwald, *J. Microencapsulation* **2000**, *17*, 177 – 185.
[12] M. Bianco, I. Viola, M. Cezza, F. Pietracaprina, G. Gigli, R. Rinaldi, V. Arima, *Microfluid. Nanofluid.* **2012**, *13*, 399 – 409.
[13] I. Viola, D. Pisignano, R. Cingolani, G. Gigli, *Anal. Chem.* **2005**, *77*, 591 – 595.
[14] A. Darhuber, S. Troian, W. Reisner, *Phys. Rev. E* **2001**, *64*, 031603:1 – 8.
[15] K. Yeo, S. Dong, E. Climent, M. R. Maxey, *Int. J. Multiphase Flow* **2010**, *36*, 221 – 233.

Received: April 19, 2014
Published online on June 11, 2014

